Modeling of Coupled Harmonic Current Source for Grid-Connected Inverters

Shun Tao, *Member, IEEE*, Xinyi Zhu, Shaobo Xu, and Yonghai Xu, *Member, IEEE*

***Abstract*—Power systems are entering the era of high proportions of new energy and power electronic equipment. The interaction between grid background harmonics and grid-connected inverters (GCIs) leads to frequency coupling effect, which results in additional frequency components injecting into the power networks. However, there is limited research on the modeling of harmonic sources based on the frequency coupling effects. Hence, this article, first, analyzes the harmonic response and emission mechanisms of frequency coupling effect caused by *dq*-axis asymmetric control of GCIs. Then, the transmission process of harmonic components in sampling delay progress, outer loop, inner loop, phase-locked loop, signal modulation module, and filter of the inverter is deduced. Voltage-controlled coupled harmonic current source models are established considering the frequency coupling effect, suitable for harmonic/interharmonic power flow studies of public supply networks. The proposed models are verified by time-domain simulations under different single harmonic and by hardware-in-the-loop simulations under multiple harmonics. Finally, the impacts of the outer loop, inner loop, phase-locked loop and output power, and the characteristics of harmonic admittance are analyzed.**

***Index Terms*—Coupled harmonic current source model, *dq*-axis asymmetric control, frequency coupling effect, grid-connected inverter.**

NOMENCLATURE

U_s	Nominal line voltage of power grid.
u_{gx}	Background harmonics in the power grid.
u_{n0}, u_{nx1}, u_{nx2}	Fundamental component, background harmonic frequency component, and coupling component of the voltage at the point of common coupling (PCC).
U_{mn0}, U_{mnx1}, U_{mnx2}	Magnitude of u_{n0}, u_{nx1}, and u_{nx2}.
i_{n0}, i_{nx1}, i_{nx2}	Fundamental component, background harmonic frequency component, and coupling frequency component of the grid-connected current at the PCC.
I_{mn0}, I_{mnx1}, I_{mnx2}	Magnitude of i_{n0}, i_{nx1}, i_{nx2}.
i_{C0}, i_{Cx1}, i_{Cx2}	Fundamental component, background harmonic frequency component, and coupling frequency component of the filter capacitor's current.
I_{mC0}, I_{mCx1}, I_{mCx2}	Magnitude of i_{C0}, i_{Cx1}, and i_{Cx2}.
u_{C0}, u_{Cx1}, u_{Cx2}	Fundamental component, background harmonic frequency component, and coupling frequency component of the filter capacitor's voltage.
φ_{un0}, φ_{unx1}, φ_{unx2}	Initial phase angles of u_{n0}, u_{nx1}, and u_{nx2}.
φ_{in0}, φ_{inx1}, φ_{inx2}	Initial phase angles of i_{n0}, i_{nx1}, and i_{nx2}.
φ_{iC0}, φ_{iCx1}, φ_{iCx2}	Initial phase angles of i_{C0}, i_{Cx1}, and i_{Cx2}.
u_{p0}, u_{px1}, u_{px2}	Fundamental component, background harmonic frequency component, and coupling frequency component of the inverter port voltage.
$u_{d\mathrm{n0}}$, $u_{q\mathrm{n0}}$	*d*-axis and *q*-axis components of u_{n0}.
$u_{d\mathrm{nx}}$, $u_{q\mathrm{nx}}$	*d*-axis and *q*-axis harmonic components of the voltages at PCC.
$i_{d\mathrm{n0}}$, $i_{q\mathrm{n0}}$	*d*-axis and *q*-axis components of i_{n0}.
$i_{d\mathrm{nx}}$, $i_{q\mathrm{nx}}$	*d*-axis and *q*-axis harmonic components of the currents at PCC.
$i_{d\mathrm{C0}}$, $i_{q\mathrm{C0}}$	*d*-axis and *q*-axis components of i_{C0}.
$i_{d\mathrm{Cx}}$, $i_{q\mathrm{Cx}}$	*d*-axis and *q*-axis harmonic components of the currents of filter capacitor.
P	Active power of GCI at PCC.
Q	Reactive power of GCI at PCC.
P_{x}	Harmonic component of *P*.
Q_{x}	Harmonic component of *Q*.
$i_{d\mathrm{ref0}}$, $i_{q\mathrm{ref0}}$	Current reference values of the inner loop generated by fundamental components.
$i_{d\mathrm{refx}}$, $i_{q\mathrm{refx}}$	Current reference values of the inner loop generated by harmonic components.
$u_{d\mathrm{ref0}}$, $u_{q\mathrm{ref0}}$	Voltage reference values for the inner loop output generated by $i_{d\mathrm{ref0}}$ and $i_{q\mathrm{ref0}}$.
$u_{d\mathrm{refx}}$, $u_{q\mathrm{refx}}$	Voltage reference values for the inner loop output generated by $i_{d\mathrm{refx}}$ and $i_{q\mathrm{refx}}$

Manuscript received 22 May 2024; revised 19 June 2024; accepted 4 July 2024. Date of publication 9 July 2024; date of current version 4 September 2024. This work was supported by the National Natural Science Foundation of China under Grant 52377101. Recommended for publication by Associate Editor D. Dujic. *(Corresponding author: Shun Tao.)*

The authors are with the State Key Laboratory of Alternate Electrical Power System with Renewable Energy Sources, North China Electric Power University, Beijing 102206, China (e-mail: taoshun@ncepu.edu.cn; 120222201733@ncepu.edu.cn; 20192101011@ncepu.edu.cn; xuyonghai@ncepu.edu.cn).

Color versions of one or more figures in this article are available at https://doi.org/10.1109/TPEL.2024.3424889.

Digital Object Identifier 10.1109/TPEL.2024.3424889

f_0, f_{x1}, f_{x2}	Fundamental frequency, background harmonic frequency component, and coupling frequency.
$\omega_0, \omega_{x1}, \omega_{x2}$	Angular frequencies corresponding to the fundamental frequency, background harmonic frequency component, and coupling frequency.
θ_0, θ_x	Fundamental and harmonic components output from the phase-locked loop (PLL).
H_{in}	Transfer function of inner loop.
H_{out}	Transfer function of out loop.
H_{PLL}	Transfer function of PLL.
L_1, R_1	Inductance and resistance of *LCL* filter on the inverter side.
L_2, R_2	Inductance and resistance of *LCL* filter on the grid side.
C, R_C	Filtering capacitor and its additional resistance.
Z_g	Grid impedance.
K_i	Current decoupling coefficient.
K_n	Coefficient for voltage feedforward compensation.
K_C	Coefficient for capacitor current feedback.

The capitalized and italicized bold letters in the text indicate the phasor form of the corresponding variables.

I. Introduction

FOLLOWING the Paris Agreement of 2015, the proportion of integration of new energy generation systems into power grids is progressively increasing [1]. The grid-connected devices mainly composed of inverters are crucial links for connecting new energy generation systems to power grids [2]. The interaction between background harmonics of power grids and grid-connected inverters (GCI) not only causes additional harmonic components, leading to harmonic pollution of the power grid [3], [4], but also may cause system resonance problems [5], [6], endangering the safety of power grids and equipment. Therefore, accurate modeling of GCI harmonic characteristics under background harmonics is of great significance for harmonic/interharmonic flow studies and resonance analysis in the coming power systems.

Domestic and foreign scholars have conducted certain research on the modeling of inverters. With regard to the native harmonics of inverters, Jiao et al. [7] presented a quantitative analysis method for dead-time harmonics based on the switching angle function. Guest et al. [8] established a sequence component harmonic model that reflected dead-time harmonics and pulse width modulation (PWM) harmonics. Xie et al. [9] developed a mathematical model that reflected the low-frequency and switching-frequency harmonics of the inverter itself. Regarding the interaction with background harmonics, Xu et al. [10] discussed the modeling of harmonic currents in grid-side inverters for direct-drive wind turbines under low-frequency harmonics in the grid and dead-zone disturbances.

In the aforementioned research on harmonic source modeling, a background harmonic voltage at a certain frequency and phase sequence could only generate the current response at the same frequency and phase sequence. They can be all called single-frequency harmonic source models of GCIs. However, due to the asymmetry of *dq*-axis control of GCI, frequency coupling effect occurs and the secondary harmonic frequency is induced [11], [12]. Once it approaches the system resonance point, a resonance amplification effect will be triggered and harmonic pollution, thus, further exacerbate. Therefore, the frequency coupling effect needs to be considered for the harmonic source modeling of GCI.

Research on the frequency coupling effects of GCI model mainly includes harmonic modeling and impedance modeling for system stability analysis in the field of electrical engineering. In terms of harmonic modeling, Xu et al. [13] analyzed the generation and frequency coupling mechanisms of the secondary harmonic components of the sampling and PWM sideband, and obtained a quantitatively analytical model of the secondary harmonic currents. However, the influence of *dq*-axis control asymmetry was not taken into account. Gao et al. [14] established the harmonic model of GCI taking into account the control asymmetry of the outer loop and inner loop, acting as an impedance. However, the impact of harmonic components on the phase-locked loop (PLL) of the inverter was not analyzed. In terms of impedance modeling of GCI, Xu et al. [10], Ye et al. [15], Liu et al. [16], Nian et al. [17], Wang et al. [18], and Sun et al. [19] established the two-frequency coupled impedance models for system stability studies; Ye et al. [15] and Wang et al. [18] ignored the further influenced of the coupled harmonics to control loops' outputs; Xu et al. [10], Liu et al. [16], and Nian et al. [17] did not achieve decoupling between the two-frequency harmonics, unsuitable for harmonic power flow studies; Sun et al. [19] ignored the influence of harmonic components on PLL, resulting in slight deviations; Xu et al. [10], Ye et al. [15], Liu et al. [16], Nian et al. [17], Wang et al. [18], and Sun et al. [19] lack the consideration of sampling and delay progress, which is inevitable and will alter the system's output characteristics for the actual GCI systems using digital controllers [20].

In this article, the voltage-controlled coupled harmonic current source models are proposed considering the frequency coupling effects under medium to low-frequency (up to 2500 Hz, which are studied in harmonic flow analysis of public power network) background harmonics in both positive and negative sequences. The models simultaneously consider the transmission processes of two-frequency coupled harmonics in the inverter control loop and additionally incorporate the influence of sampling delay, improving the accuracy of the models.

The harmonic components of the GCI grid-connected current at the background harmonic frequency and the coupled harmonic frequency can be calculated with disturbance frequency voltage at PCC, respectively. The model considers the mutual influence between the two-frequency currents simultaneously, called two-frequency coupled harmonic current source models. The main

TABLE I
COMPARISON OF DIFFERENT MODELS

Source	frequency	Model types	Aspects considered ①	②	③	④	Application field
This article	≤ 2500 Hz	C-C	✓	✓	✓	✓	Harmonic analysis
[14]	≥100 Hz	C-I		✓	✓		Stability studies
[15]	≥100 Hz	C-I	✓	✓			Stability studies
[16]	≥100 Hz	C-I	✓	✓			Stability studies
[17]	≤ 100 Hz	C-I	✓	✓	✓		Stability studies
[18]	≥100 Hz	C-I	✓	✓	✓		Stability studies
[19]	≤100 Hz	C-I	✓	✓	✓		Stability studies
[20]	≥100 Hz	C-I	✓	✓			Stability studies

Note: ① represents PLL, ② represents inner loop, ③ represents outer loop, and ④ represents the sampling and delay progress; C-C represents coupled current model and C-I represents coupled impedance/admittance model.

characteristics of the new models over the existing methods are as follows.

1) They take into account the secondary currents induced by frequency coupling effect which mainly functions for frequencies below 1000 Hz.
2) They are linear models under steady-state conditions.
3) They are current source models controlled by the harmonic voltages at PCC and the harmonic currents at same frequency, generated from different background harmonics, can be vectorially superimposed. Hence, they can be readily integrated into existing harmonic power flow tools.

The comparison of the work in this paper with those in other references is shown in Table I.

The rest of this article is organized as follows. Section II analyzes the emission mechanism of the background harmonic frequency current and coupling frequency current. Section III presents the detailed derivation of the two-frequency coupled harmonic current source models of GCI. Section IV verifies the correctness of the models under different single background harmonic with time-domain simulations and the adaptability of the models under multiple background harmonics with hardware-in-the-loop (HIL) simulations. The influencing factors of the models and the harmonic admittance characteristics of GCI are analyzed in Section V. Finally, Section VI concludes this article.

II. HARMONICS CAUSED BY CONTROL ASYMMETRY UNDER BACKGROUND HARMONIC

Fig. 1 depicts the structure frame of GCI, including the main circuit and control circuit. From Fig. 1, it can be seen that GCI in this article adopts a control strategy with current inner loop and power outer loop, obtaining the voltage phase at PCC through PLL. Though there are more advanced PLL algorithms, such as decoupled double synchronous reference frame (SRF) PLL [21], SRF-PLL is more generally used in impedance modeling [10], [15], [16], [17], [18], [19], [22], and is studied in the article. Under the condition of symmetric inputs in the control system, there exist three aspects of asymmetry in the *dq* control system [17], [11].

1) The input to PLL consists only of the q-axis voltage u_{qn}.

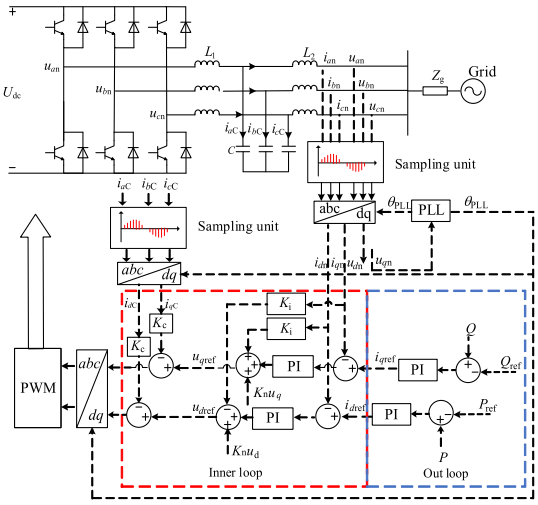

Fig. 1. Topology structure and control elements of GCI connected power grid.

2) The inputs to the inner loop are unequal because of the difference of active and reactive power controllers [23].
3) The structure of inner loop controller control is asymmetric.

The fundamental components $\boldsymbol{X}(f_0)$ in positive sequence in the three-phase stationary coordinate system are changed into dc components, X_{d0} and X_{q0}, being relatively stationary in the *dq* coordinate system, as shown in Fig. 2(a). Even if the magnitudes of *d*- and *q*-axes components are unequal, no new frequency component is produced after inverse Park transformation to the three-phase coordinate system except the fundamental components.

Symmetrical input harmonic components $\boldsymbol{X}_{\mathrm{in}}(f_{\mathrm{x}})$ in positive sequence in the three-phase stationary coordinate system are changed into symmetrical rotating components X_{q_in} and X_{d_in} at $f_{\mathrm{x}} - f_0$, as shown in Fig. 2(b). After such symmetrical rotating components are inversely transformed to the three-phase stationary coordinate system, only harmonic components with the frequency f_{x} exist.

However, after passing through the asymmetric control stages of GCI, symmetric inputs along the *dq*-axis will yield asymmetric outputs of *dq*-axis, X_{q_out} and X_{d_out}, as illustrated in Fig. 2(c). The asymmetric outputs can be decomposed into two sets of symmetric components. One set is the components $\boldsymbol{X}_{\mathrm{out1}}$ in the same rotating direction at $f_{\mathrm{x}} - f_0$, as shown in Fig. 2(d), and the other set is the components $\boldsymbol{X}_{\mathrm{out2}}$ in the inverse rotating direction at $f_{\mathrm{x}} - f_0$, which are in the same rotating direction at $f_0 - f_{\mathrm{x}}$ [24], as shown in Fig. 2(e). A component with frequency f is equivalent to the conjugate of a component with frequency $-f$ in the frequency domain [25]. Therefore, the symmetric components with rotating frequency $f_{\mathrm{x}} - f_0$ correspond to those with the frequency f_{x} in the three-phase stationary coordinate system after inverse transformation, while the symmetric components with rotating frequency $f_0 - f_{\mathrm{x}}$ correspond to those with the frequency $2f_0 - f_{\mathrm{x}}$ in positive sequence or $f_{\mathrm{x}} - 2f_0$ in negative sequence in the three-phase stationary coordinate system.

Therefore, it is seen that the response currents of GCI have the components at f_{x} in positive sequence and the components

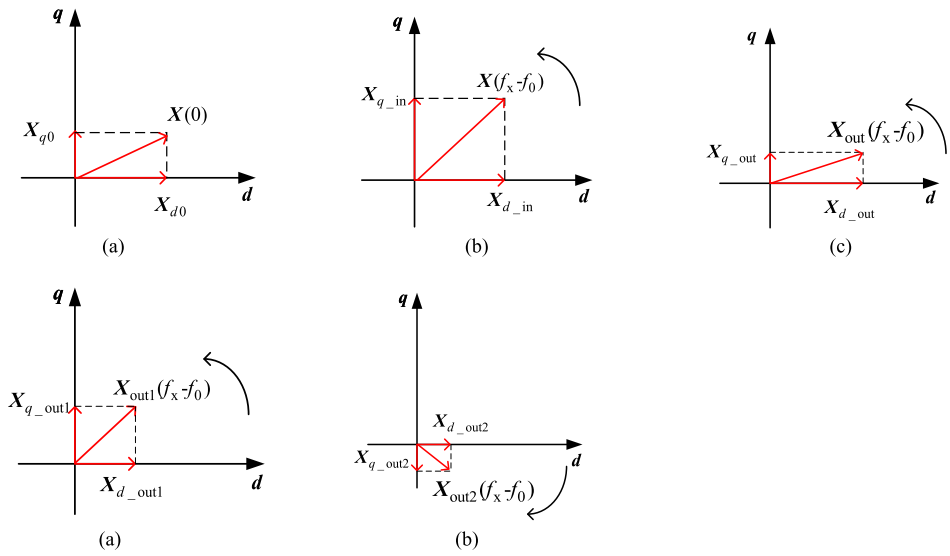

Fig. 2. Mechanism of frequency coupling effect. (a) Fundamental component $X(f_0)$. (b) Symmetrical input $X_{\rm in}(f_{\rm x})$. (c) Asymmetrical output $X_{\rm out}(f_{\rm x})$. (d) Symmetrical output $X_{\rm out1}(f_{\rm x})$. (e) Symmetrical output $X_{\rm out2}(f_{\rm x}\text{-}2f_0)$.

TABLE II
CORRESPONDENCE BETWEEN BACKGROUND VOLTAGE COMPONENTS AND RESPONSE CURRENT COMPONENTS

Scenarios	Frequency of background voltage	Response currents	
		Background harmonic frequency	Coupled frequency
Sce I	$f_{\rm x}$ ($f_{\rm x}$>2f_0) (+)	$f_{\rm x}$ (+)	$f_{\rm x}$-2f_0 (-)
Sce II	$f_{\rm x}$ ($f_{\rm x}$<2f_0) (+)	$f_{\rm x}$ (+)	2f_0-$f_{\rm x}$ (+)
Sce III	$f_{\rm x}$ (-)	$f_{\rm x}$ (-)	$f_{\rm x}$+2f_0 (+)

Note: (+) represents positive sequence and (-) represents negative sequence.

at $f_{\rm x} - 2f_0$ in negative sequence under the excitation of background harmonic voltages at $f_{\rm x}$ in positive sequence because of the asymmetric control stages of GCI. This is the frequency coupling effect. Similarly, the response currents of GCI have the components at $f_{\rm x}$ in negative sequence and the components at $f_{\rm x} + 2f_0$ in positive sequence under the excitation of background harmonic voltages at $f_{\rm x}$ in negative sequence.

According to the relationships of coupled frequencies, the disturbance frequency range and the sequence characteristics, there are three scenarios for the background harmonic voltages and the response harmonic currents of GCI, summarily shown in Table II.

III. TWO-FREQUENCY COUPLED HARMONIC CURRENT SOURCE MODELS

A. Harmonic Current Source Modeling in Sce I

According. to the conclusion in Sce I of Table II, taking phase *a* as an example, when the grid is subjected to a positive-sequence background *harmonic* $\boldsymbol{U}_{agx}$ with a frequency $f_{\rm x1}$ ($f_{\rm x1}$>2f_0), the voltage at PCC is expressed as

$$u_{an} = u_{\rm an0}+u_{\rm anx1} + u_{\rm anx2}$$

$$\begin{cases} u_{an0} = U_{\rm mn0}\cos(\omega_0 t + \varphi_{\rm un0}) \\ u_{\rm anx1} = U_{\rm mnx1}\cos(\omega_{\rm x1} t + \varphi_{\rm unx1}) \\ u_{\rm anx2} = U_{\rm mnx2}\cos(\omega_{\rm x2} t + \varphi_{\rm unx2}). \end{cases} \tag{1}$$

After the sampling delay process, the grid-connected voltage can be expressed as

$$u'_{\rm an} = u_{\rm an0}e^{-1.5{\rm j}T_{\rm s}\omega_0}+u_{\rm anx1}e^{-1.5{\rm j}T_{\rm s}\omega_{\rm x1}} + u_{\rm anx2}e^{-1.5{\rm j}T_{\rm s}\omega_{\rm x2}} \tag{2}$$

where $T_{\rm s}$ represents the sampling period. Equation (2) takes into account the sampling delay, which is usually set to 1.5 $T_{\rm s}$ [26].

The grid-connected current and the filter capacitor current can be expressed in the same way, as shown in (1) and (2).

The harmonic components of the grid-connected voltages and currents are transformed into *dq*-axis components, denoted as $\boldsymbol{U}_{d\rm nx}$ and $\boldsymbol{U}_{q\rm nx}$ in (3), respectively, in the control stage using Park's transformation matrix $\mathbf{P}(\theta_{\rm PLL})$. $\mathbf{P}(\theta_{\rm PLL})$ is equal to the product of the harmonic component transformation matrix $\mathbf{P}_{\mathbf{x}}(\theta_{\mathbf{x}})$ and the fundamental component transformation matrix $\mathbf{P}(\theta_0)$ [27], [28]. The specific forms of the transformation matrices can be found in Appendix A

$$\begin{cases} \boldsymbol{U}_{d\rm nx} = \boldsymbol{U}_{\rm anx1}e^{-1.5{\rm j}T_{\rm s}(\omega_{\rm x1}-\omega_0)} + \boldsymbol{U}^*_{\rm anx1}e^{-1.5{\rm j}T_{\rm s}(\omega_{\rm x1}-\omega_0)} \\ \boldsymbol{U}_{q\rm nx} = -{\rm j}\boldsymbol{U}_{\rm anx1}e^{-1.5{\rm j}T_{\rm s}(\omega_{\rm x1}-\omega_0)} \\ \quad +{\rm j}\boldsymbol{U}^*_{\rm anx1}e^{-1.5{\rm j}T_{\rm s}(\omega_{\rm x1}-\omega_0)} - U_{\rm mn0}\boldsymbol{\theta}_{\rm x} \end{cases} \tag{3}$$

where "$*$" represents the conjugate of a phasor.

The input to PLL is the measurement value of the *q*-axis voltage u_{qn}. Hence, PLL will be affected by the harmonic voltage. The output of PLL includes not only the fundamental component but also the harmonic component with a frequency of $f_{\rm x1}$-f_0, as shown in

$$\theta_{\rm PLL} = \theta_0 + \theta_{\rm x} \tag{4}$$

$\boldsymbol{\theta}_{\mathrm{x}}$ can be solved by combining PLL expression, as shown in

$$\boldsymbol{\theta}_{\mathrm{x}}=\frac{H_{PLL}(\mathrm{j}(\omega_{\mathrm{x1}}-\omega_0))e^{-1.5\mathrm{j}T_{\mathrm{s}}(\omega_{\mathrm{x1}}-\omega_0)}(-\mathrm{j}\boldsymbol{U}_{anx1}+\mathrm{j}\boldsymbol{U}_{anx2})}{\mathrm{j}(\omega_{\mathrm{x1}}-\omega_0)+U_{\mathrm{mn0}}H_{PLL}(\mathrm{j}(\omega_{\mathrm{x1}}-\omega_0))}. \tag{5}$$

Similarly, the harmonic components $\boldsymbol{I}_{dnx}$ and $\boldsymbol{I}_{qnx}$ as well as $\boldsymbol{I}_{dcx}$ and $\boldsymbol{I}_{qcx}$ can be obtained.

The system adopts a power outer loop controller, where the active and reactive power output by the inverter track the three-phase power setpoints. The relationship between the three-phase power and the *dq*-axis voltage and current in the control stage can be expressed by

$$\begin{bmatrix}P\\Q\end{bmatrix}=\frac{3}{2}\begin{bmatrix}u_{dn}i_{dn}+u_{qn}i_{qn}\\u_{qn}i_{dn}-u_{dn}i_{qn}\end{bmatrix}. \tag{6}$$

Extracting harmonic components from P and Q, as shown in

$$\begin{bmatrix}\boldsymbol{P}_{\mathrm{x}}\\\boldsymbol{Q}_{\mathrm{x}}\end{bmatrix}=\frac{3}{2}\times\begin{bmatrix}U_{\mathrm{mn0}}\boldsymbol{I}_{anx1}+U_{\mathrm{mn0}}\boldsymbol{I}^{*}_{anx2}+\boldsymbol{U}_{anx1}\boldsymbol{I}^{*}_{an0}+\boldsymbol{I}_{an0}\boldsymbol{U}^{*}_{anx2}\\\mathrm{j}U_{\mathrm{mn0}}\boldsymbol{I}_{anx1}-\mathrm{j}U_{\mathrm{mn0}}\boldsymbol{I}^{*}_{anx2}-\mathrm{j}\boldsymbol{U}_{anx1}\boldsymbol{I}^{*}_{an0}+\mathrm{j}\boldsymbol{I}_{an0}\boldsymbol{U}^{*}_{anx2}\end{bmatrix}. \tag{7}$$

The current inner loop controller controls the *dq*-axis currents i_{dn} and i_{qn} to track the current reference values i_{dref} and i_{qref} output by the power outer loop controller. Therefore, i_{dn0} and i_{qn0} have the same numerical values as i_{dref0} and i_{qref0}, respectively, as shown in (8). The harmonic components $\boldsymbol{I}_{drefx}$ and $\boldsymbol{I}_{qrefx}$ can be deduced from the structural diagram of the power outer loop in Fig. 1, as shown in (9)

$$\begin{bmatrix}i_{dref0}\\i_{qref0}\end{bmatrix}=\begin{bmatrix}i_{dn0}\\i_{qn0}\end{bmatrix}=\begin{bmatrix}I_{\mathrm{mn0}}\cos(\varphi_{\mathrm{in0}})\\I_{\mathrm{mn0}}\sin(\varphi_{\mathrm{in0}})\end{bmatrix} \tag{8}$$

$$\begin{bmatrix}\boldsymbol{I}_{drefx}\\\boldsymbol{I}_{qrefx}\end{bmatrix}=H_{\mathrm{OUT}}(\mathrm{j}(\omega_{\mathrm{x1}}-\omega_0))\begin{bmatrix}-\boldsymbol{P}_{\mathrm{x}}\\\boldsymbol{Q}_{\mathrm{x}}\end{bmatrix}. \tag{9}$$

The dc components u_{dref0} and u_{qref0}, as well as the harmonic components $\boldsymbol{U}_{drefx}$ and $\boldsymbol{U}_{qrefx}$ of the *dq*-axis voltage reference values output by the current inner loop can be deduced from the structural diagram of the current inner loop with the voltage feedforward compensation and the capacitor current feedback, as shown in

$$\begin{cases}u_{dref0}=H_{\mathrm{IN}}(\mathrm{j}\omega_0)(i_{dref0}-i_{dn0})-K_{\mathrm{i}}i_{qn0}+K_{\mathrm{n}}u_{dn0}\\\qquad -K_{\mathrm{C}}i_{dC0}\\\qquad =-K_{\mathrm{i}}I_{\mathrm{mn0}}\sin(\varphi_{\mathrm{in0}})+U_{\mathrm{mn0}}-K_{\mathrm{C}}i_{dC0}\\u_{qref0}=H_{\mathrm{IN}}(\mathrm{j}\omega_0)(i_{qref0}-i_{q0})+K_{\mathrm{i}}i_{dn0}+K_{\mathrm{n}}u_{qn0}\\\qquad -K_{\mathrm{C}}i_{qC0}\\\qquad =K_{\mathrm{i}}I_{\mathrm{mn0}}\cos(\varphi_{\mathrm{in0}})-K_{\mathrm{C}}i_{qC0}\end{cases} \tag{10}$$

$$\begin{cases}\boldsymbol{U}_{drefx}=H_{\mathrm{IN}}(\mathrm{j}(\omega_{\mathrm{x1}}-\omega_0))(\boldsymbol{I}_{drefx}-\boldsymbol{I}_{dnx})-K_{\mathrm{C}}\boldsymbol{I}_{dCx}\\\quad -K_{\mathrm{i}}\boldsymbol{I}_{qnx}+K_{\mathrm{n}}\boldsymbol{U}_{dnx}\\\boldsymbol{U}_{qrefx}=H_{\mathrm{IN}}(\mathrm{j}(\omega_{\mathrm{x1}}-\omega_0))(\boldsymbol{I}_{qrefx}-\boldsymbol{I}_{qnx})-K_{\mathrm{C}}\boldsymbol{I}_{qCx}\\\quad +K_{\mathrm{i}}\boldsymbol{I}_{dnx}+K_{\mathrm{n}}\boldsymbol{U}_{qnx}.\end{cases} \tag{11}$$

The *dq*-axis voltage reference values $\boldsymbol{U}_{dref}$ and $\boldsymbol{U}_{qref}$ are the superposition of their direct components and harmonic components, as shown in

$$\begin{bmatrix}\boldsymbol{U}_{dref}\\\boldsymbol{U}_{qref}\end{bmatrix}=\begin{bmatrix}u_{dref0}+\boldsymbol{U}_{drefx}\\u_{qref0}+\boldsymbol{U}_{qrefx}\end{bmatrix}. \tag{12}$$

$\boldsymbol{U}_{dref}$ and $\boldsymbol{U}_{qref}$ are transformed into the harmonic components of the voltage at the inverter's port through the Park's inverse transformation matrix $\mathbf{P}^{-1}(\theta_{\mathrm{PLL}})$ [27], [28] (seen in Appendix A) and the modulation process, as shown in (13). The specific equations of coefficients A_{ij} in (17) can be found in Appendix (B.1)

$$\begin{cases}\boldsymbol{U}_{apx1}=A_{11}\boldsymbol{I}_{anx1}+A_{12}\boldsymbol{U}_{anx1}+A_{13}\boldsymbol{U}_{anx2}+A_{14}\boldsymbol{\theta}_{\mathrm{x}}\\\boldsymbol{U}_{apx2}=A_{21}\boldsymbol{I}_{anx2}+A_{22}\boldsymbol{U}_{anx2}+A_{23}\boldsymbol{U}_{anx1}+A_{24}\boldsymbol{\theta}_{\mathrm{x}}\end{cases}. \tag{13}$$

Incorporating the topology of the inverter's main circuit, the equations can be derived, as shown in (14)–(16) to describe the relationships of the currents and voltages at the inverter's port, the voltages and currents at PCC, the filter capacitor, and the power grid at harmonic frequencies.

The current equations are shown in (17) according to Kirchhoff's current law.

By substituting (13)–(16) into (17), an equation can be established between the background harmonic voltage and the voltages at the background harmonic frequency and the coupled secondary frequency at the PCC. The solution is shown as (18), where the specific expression for coefficients A_{i} can be found in Appendix (B.2).

By substituting (18) into (15), (19) is obtained to represent that the harmonic response current $\boldsymbol{I}_{anx1}$ and the coupled secondary harmonic current $\boldsymbol{I}_{anx2}$, which are all the function of background harmonic voltage $\boldsymbol{U}_{anx1}$ at the PCC.

In (19), Y_{i1} and Y_{i2} are referred to as two-frequency coupling admittances. When the power grid has a certain frequency background harmonic, Y_{i1} quantifies the response degree of gird-connected current at the background harmonic frequency, referred to as self admittance, Y_{i2} quantifies the response degree of gird-connected current at the coupling harmonic frequency, referred to as transfer admittance [19], [29]

$$\begin{cases}\boldsymbol{I}_{apx1}=\frac{\boldsymbol{U}_{apx1}-\boldsymbol{U}_{acx1}}{R_1+\mathrm{j}\omega_{\mathrm{x1}}L_1}\\\boldsymbol{I}_{apx2}=\frac{\boldsymbol{U}_{apx2}-\boldsymbol{U}_{acx2}}{R_1+\mathrm{j}\omega_{\mathrm{x2}}L_1}\end{cases} \tag{14}$$

$$\begin{cases}\boldsymbol{I}_{anx1}=\frac{\boldsymbol{U}_{acx1}-\boldsymbol{U}_{anx1}}{R_2+\mathrm{j}\omega_{\mathrm{x1}}L_2}=\frac{\boldsymbol{U}_{anx1}-\boldsymbol{U}_{agx}}{R_{\mathrm{g}}+\mathrm{j}\omega_{\mathrm{x1}}L_{\mathrm{g}}}\\\boldsymbol{I}_{anx2}=\frac{\boldsymbol{U}_{acx2}-\boldsymbol{U}_{anx2}}{R_2+\mathrm{j}\omega_{\mathrm{x2}}L_2}=\frac{\boldsymbol{U}_{anx2}}{R_{\mathrm{g}}+\mathrm{j}\omega_{\mathrm{x2}}L_{\mathrm{g}}}\end{cases} \tag{15}$$

$$\begin{cases}\boldsymbol{I}_{acx1}=\frac{\boldsymbol{U}_{aCx1}}{R_{\mathrm{C}}+\frac{1}{\mathrm{j}\omega_{\mathrm{x1}}C}}\\\boldsymbol{I}_{acx2}=\frac{\boldsymbol{U}_{aCx2}}{R_{\mathrm{C}}+\frac{1}{\mathrm{j}\omega_{\mathrm{x2}}C}}\end{cases} \tag{16}$$

$$\begin{cases}\boldsymbol{I}_{apx1}=\boldsymbol{I}_{anx1}+\boldsymbol{I}_{aCx1}\\\boldsymbol{I}_{apx2}=\boldsymbol{I}_{anx2}+\boldsymbol{I}_{aCx2}\end{cases} \tag{17}$$

$$\begin{bmatrix}\boldsymbol{U}_{anx1}\\\boldsymbol{U}_{anx2}\end{bmatrix}=\begin{bmatrix}\frac{A_2A_5}{A_3A_4-A_1A_5}\\\frac{-A_2A_4}{A_3A_4-A_1A_5}\end{bmatrix}\boldsymbol{U}_{agx} \tag{18}$$

$$\begin{bmatrix}\boldsymbol{I}_{anx1}\\ \boldsymbol{I}_{anx2}\end{bmatrix}=\begin{bmatrix}\frac{A_2A_5-A_3A_4+A_1A_5}{A_2A_5(R_g+j\omega_{x1}L_g)}\\ \frac{-A_4}{A_5(R_g+j\omega_{x2}L_g)}\end{bmatrix}\boldsymbol{U}_{anx1}=\begin{bmatrix}Y_{i1}\\ Y_{i2}\end{bmatrix}\boldsymbol{U}_{anx1}. \quad (19)$$

B. Harmonic Current Source Modeling in Sce II

When the frequency of the positive-sequence background harmonic is less than twice the fundamental frequency (see Sce II in Table II), it is necessary to modify the expression for coefficient A_{ij} in (13), and then substitute it back into (19) to obtain the two-frequency harmonic current source model of GCI at the PCC in Sce II. The specific modification equations are shown in Appendix (B.3).

C. Harmonic Current Source Modeling in Sce III

For the model under negative-sequence background harmonics (see Sce III in Table II) with frequencies greater than twice the fundamental frequency, similar transfer processes yield the voltage reference values in the *dq*-axis, denoted as $\boldsymbol{U}_{dref}$ and $\boldsymbol{U}_{qref}$. After the voltage feedforward and the capacitor current feedback, they are modulated with $\mathbf{P}^{-1}(\theta_{PLL})$ and PWM modulation to obtain the harmonic components at the inverter port, as shown in (20). The coefficients B_{ij} in (20) are presented in Appendix (B.4). Considering the circuit topology, the PCC harmonic voltages and harmonic currents can be presented in (21) and (22). The coefficient B_i can be found in the Appendix (B.5). Equation (22) constitutes the emission model of harmonic current sources at PCC under negative-sequence background harmonic

$$\begin{cases}\boldsymbol{U}_{apx1}=B_{11}\boldsymbol{I}_{anx1}+B_{12}\boldsymbol{U}_{anx1}+B_{13}\boldsymbol{U}_{anx2}+B_{14}\boldsymbol{\theta}_x\\ \boldsymbol{U}_{apx2}=B_{21}\boldsymbol{I}_{anx2}+B_{22}\boldsymbol{U}_{anx2}+B_{23}\boldsymbol{U}_{anx1}+B_{24}\boldsymbol{\theta}_x\end{cases} \quad (20)$$

$$\begin{bmatrix}\boldsymbol{U}_{anx1}\\ \boldsymbol{U}_{anx2}\end{bmatrix}=\begin{bmatrix}\frac{B_2B_5}{B_3B_4-B_1B_5}\\ \frac{-B_2B_4}{B_3B_4-B_1B_5}\end{bmatrix}\boldsymbol{U}_{agx} \quad (21)$$

$$\begin{bmatrix}\boldsymbol{I}_{anx1}\\ \boldsymbol{I}_{anx2}\end{bmatrix}=\begin{bmatrix}\frac{B_2B_5-B_3B_4+B_1B_5}{B_2B_5(R_g+j\omega_{x1}L_g)}\\ \frac{-B_4}{B_5(R_g+j\omega_{x2}L_g)}\end{bmatrix}\boldsymbol{U}_{anx1}=\begin{bmatrix}Y_{i1}\\ Y_{i2}\end{bmatrix}\boldsymbol{U}_{anx1}. \quad (22)$$

For the harmonic current source model under negative-sequence background harmonic with frequencies lower than twice the fundamental frequency, the expression is the same as that of the negative-sequence model with frequencies greater than twice the fundamental frequency.

D. Characteristics of Harmonic Current Source Models

It can be observed from the derivation process of (19) and (22) that the established models of two-frequency coupled harmonic current sources are obtained under steady-state conditions. The harmonic response current and the coupled secondary harmonic current are all the functions of background harmonic frequency voltage at PCC. The harmonic at f_{x1} generates a harmonic at f_{x2} through the frequency coupling effect, and the two have opposite phase sequence. The coupled harmonic at f_{x2} generated a new coupled harmonic at f_{x1}. Therefore, the further coupling effects of coupling components do not lead to new harmonic frequencies. The frequency coupling process of GCI between the two-frequency components is depicted in Fig. 3. With the assumptions of the expressions for voltage and currents similar to (1), the establishment of steady-state model has already included the further coupling process of coupling components.

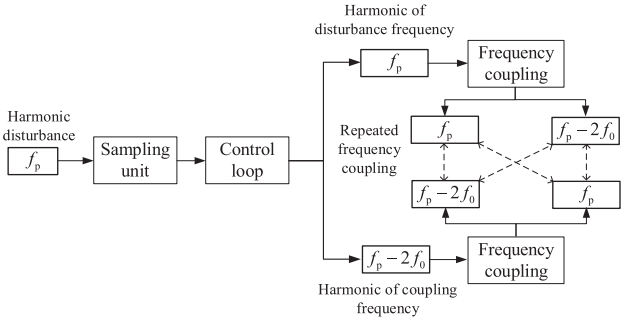

Fig. 3. Coupling process between two-frequency harmonics.

TABLE III
SIMULATION PARAMETERS

Parameter	Symbol	Numerical Value
PLL	$H_{PLL}(s)$	50+900/s
Outer loop	$H_{out}(s)$	0.1+5/s
Inner loop	$H_{in}(s)$	5+50/s
Grid voltage level	U_s	10 kV
Dc voltage	U_{dc}	20 kV
Active power set value	P_{set}	5 MW
Voltage proportional feedforward coefficient	K_n	1
Modulation degree	K_{PWM}	1
Grid equivalent inductance	L_g	3 mH
Grid equivalent resistance	R_g	0.3 Ω
Inverter-side filter inductance	L_1	6 mH
Grid-side filter inductance	L_2	5 mH
Filter capacitance	C	12 μF
Filter capacitance resistance	R_C	5 Ω

IV. Model Verification and Analysis

In this section, the proposed models are verified under different single background harmonic with time-domain simulations of MATLAB/Simulink. HIL simulations are also conducted to check the adaptability of the models under multiple background harmonics. The parameters in Fig. 1 are presented in Table III.

A. Time-Domain Simulations Verification Under Single Background Harmonic

Positive and negative-sequence background harmonics, and interharmonics are individually applied with a grid voltage

TABLE IV
GRID-CONNECTED HARMONIC CURRENTS UNDER POSITIVE-SEQUENCE BACKGROUND HARMONIC ($>2f_0$)

I_{anx1} at background harmonic order			I_{anx2} at coupling harmonic order		
Order	Calculated value (A)	Simulative value (A)	Order	Calculated value (A)	Simulative value (A)
5	66.23∠-54.59°	65.04∠-57.50°	3	22.31∠176.56°	21.08∠173.60°
7	67.34∠95.5°	66.34∠95.3°	5	19.41∠137.09°	17.18∠139.70°
9	59.67∠121.98°	58.82∠121.97°	7	13.61∠99.78°	12.55∠97.55°
11	46.27∠138.36°	47.74∠137.10°	9	10.62∠70.03°	9.96∠77.70°
13	39.36∠155.70°	39.93∠152.46°	11	8.31∠37.20°	8.4∠39.00°

TABLE V
GRID-CONNECTED HARMONIC CURRENTS UNDER NEGATIVE-SEQUENCE BACKGROUND HARMONIC ($>2f_0$)

I_{anx1} at background harmonic order			I_{anx2} at coupling harmonic order		
Order	Calculated value (A)	Simulative value (A)	Order	Calculated value (A)	Simulative value (A)
5	36.81∠-57.95°	35.7∠-63.82°	7	26.87∠116.21	26.24∠111.83°
7	42.86∠-78.24°	41.63∠-78.55°	9	20.98∠69.11°	18.51∠66.56°
9	46.39∠96.64°	46.99∠94.60°	11	13.40∠28.81°	12.43∠30.94°
11	53.28∠116.89°	53.93∠114.80°	13	8.20∠-16.02°	8.18∠-16.01°
13	51.07∠132.45°	52.21∠131.64°	15	4.18∠-52.98°	4.10∠-47.20°

TABLE VI
GRID-CONNECTED HARMONIC CURRENTS UNDER INTERHARMONIC ($<2f_0$)

I_{anx1} at background harmonic frequency			I_{anx2} at coupling harmonic frequency		
Frequency (Hz)	Calculated value (A)	Simulative value (A)	Frequency (Hz)	Calculated value (A)	Simulative value (A)
95	25.36	24.49	5	29.79	28.78
90	23.86	23.13	10	30.39	29.57
80	20.92	20.33	20	32.27	31.37
75	19.41	18.20	25	33.52	32.24
70	17.90	16.99	30	35.33	33.37

0.1 p.u. and a phase angle of 90°. The calculating results with the models and the simulation results under the single background harmonic are presented in Tables IV, V, and VI. All calculation and simulation results are in amplitude.

It can be seen from the Tables that the calculated values and the simulated values are close, which confirms the accuracy of the two-frequency coupled harmonic current source models under single positive and negative-sequence background harmonic and interharmonic.

B. HIL Simulation Validation Under Multiple Harmonics

Background harmonic in power systems often consists of multiple harmonic frequencies. Therefore, a HIL simulation platform is applied to verify the accuracy and adaptability of the model under composite background harmonics.

The HIL simulation platform, shown in Fig. 4 consists of an RT-BOX hardware simulator, a physical digital signal processor (DSP) controller (TMS320F28069), and an external computer device. The DSP controller is used to implement the voltage/current sampling, controlling, and PWM signal generation process. A symmetrical rule based PWM modulation method is adopted. The three-phase currents waveforms of the inverter at the PCC are sequentially recorded by an oscilloscope. The frequency spectrums of currents are obtained with FFT analysis. The waveforms in three-phase and the analysis results in phase A is shown in Fig. 5 as an example, where the background harmonic component is positive sequence and its frequency is set to 350 Hz (7th) with an amplitude of 0.1 p.u.

Multiple harmonics including 5th to 13th odd-order positive sequence with amplitudes of 0.05 p.u. are applied to the grid voltage simultaneously. The calculated values of $\boldsymbol{I}_{anx1}$ and $\boldsymbol{I}_{anx2}$ corresponding to each order are obtained by (19), and then those at the same frequency order are superimposed with phase angle. The calculated harmonic current and experimental current from the HIL simulation platform at each order are shown in Table VII. In the table, the numbers in parentheses represent the harmonic components at each order,

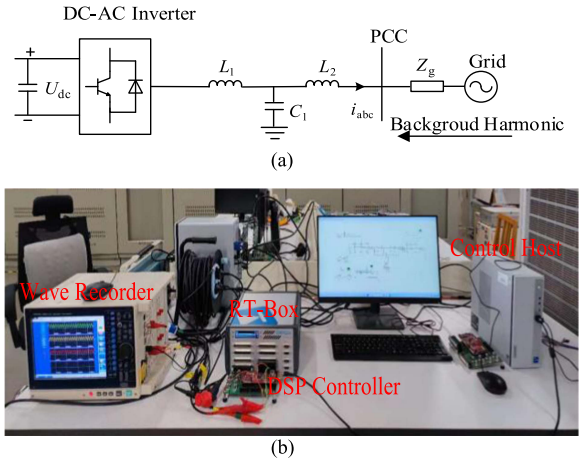

Fig. 4. Experimental verification platform. (a) Experimental schematic diagram. (b) Hardware-in-the-loop test platform.

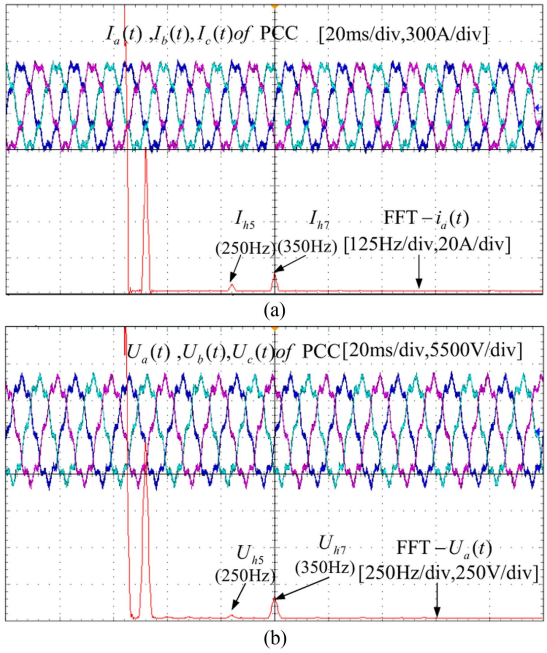

Fig. 5. Experimental platform results under positive-sequence background harmonics. (a) Oscilloscope waveforms of grid-connected currents. (b) Oscilloscope waveforms of PCC voltages.

TABLE VII
GRID-CONNECTED HARMONIC CURRENTS UNDER MULTIPLE POSITIVE SEQUENCE HARMONICS

Order	Superimposed calculated value (A)	Experimental value (A)
$3(3_5)$	10.40	10.44
$5(5+5_7)$	22.57	24.44
$7(7+7_9)$	25.04	26.79
$9(9+9_{11})$	22.67	23.71
$11(11+11_{13})$	19.46	21.99
13	19.43	19.38

TABLE VIII
GRID-CONNECTED HARMONIC CURRENTS UNDER MULTIPLE POSITIVE AND NEGATIVE-SEQUENCE HARMONICS

Order	Superimposed calculated value (A)	Experimental value (A)
5_5+5_7	18.96	19.56
7_5+7_7	46.87	47.51

and the subscripts represent the coupling effect between the corresponding frequency harmonics. The calculated values and the experimental values are close, proving the adaptability of the proposed models under multiple background harmonics.

Taking into account the phase sequence characteristics of different symmetrical harmonics, multiple harmonics of fifth negative sequence and seventh positive sequence with an amplitude of 0.1 p.u. are simultaneously applied to the grid. The calculated values can be obtained by (19) and (22). The comparison results are shown in Table VIII. The calculated values are in close agreement with the experimental values. It is verified from Tables VII and VIII that the harmonic currents at the same frequency calculated with the proposed models under multiple harmonics can be vectorially superimposed.

In the HIL simulations, the amplitudes of background harmonics increase from 0.025 p.u. to 0.1 p.u. The harmonic voltage and harmonic current at PCC are measured, which are used to calculate the experimental values of the admittances in (19) and (22). The experimental values of Y_{i1} and Y_{i2} are invariable with the change of magnitudes of background harmonic, which means that the models are linear.

V. ANALYSIS OF INFLUENCING FACTORS ON MODELS

A. Harmonic Impact Factor Analysis

In the previous section, the correctness of the models has been verified based on the digital simulation and hardware experimentations. Further discussion is required to identify specific factors that affect the harmonic currents at PCC.

1) Bandwidth of Frequency Coupling Effect: The magnitude curves of $\boldsymbol{I}_{\mathrm{anx1}}$ and $\boldsymbol{I}_{\mathrm{anx2}}$ are obtained based on the calculations and the simulations under single 5th–51st odd-order positive-sequence background harmonics and 3rd–49th odd-order negative-sequence background harmonics with grid voltage magnitude of 0.1 p.u., as shown in Fig. 6. In Fig. 6, it can be observed that when the harmonic frequency is low, the coupling current cannot be ignored. In a particular case, when the third negative-sequence background harmonics are applied, the magnitude of I_{anx2} even exceeds I_{anx1}. As the frequency increases, the coupling currents gradually decrease, and at approximately 1000 Hz, the magnitude of the coupling currents will be less than one-tenth of the currents at the background harmonic order, hence, it can be negligible. Additionally, it can also be seen from Fig. 7 that the models established in this article exhibit good adaptability in the mid-to-low frequency range, enabling accurate calculation of background harmonic frequency currents and coupling currents.

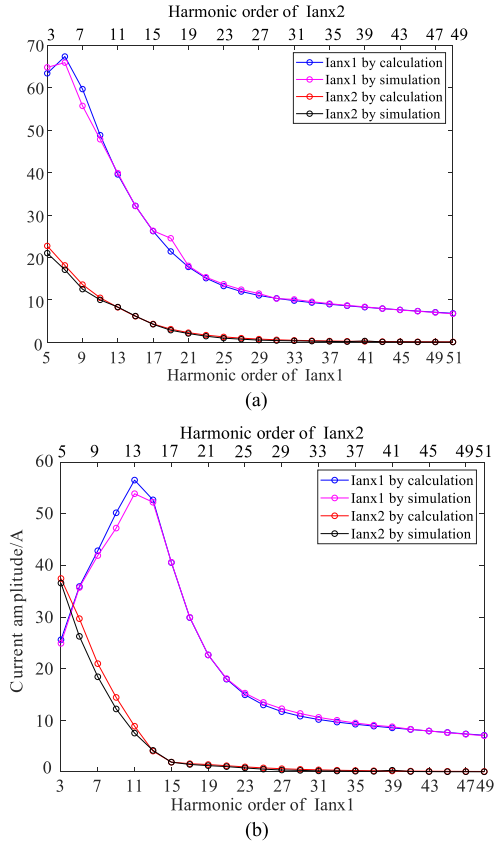

Fig. 6. Comparison of calculation with simulation. (a) Positive sequence. (b) Negative sequence.

2) Impacts of Sampling Delay Process: Under the conditions with and without the sampling delay progress, the comparisons of current responses with 5th–21st odd-order positive-sequence background harmonic disturbances are shown in Fig. 7. It can be observed from Fig. 7 that the sampling delay has a significant impact on the calculated results of the two-frequency currents. If sampling delay is not considered in the modeling process, it will not only lead to errors in the calculation of current responses but also further impact the subsequent analysis of model influencing factors. Hence, in order to make the model more closely aligned with engineering reality, the sampling delay must be considered during the modeling process.

3) Impacts of Inner Loop Control Parameters: The impacts of inner loop control parameters are shown in Fig. 8. It can be observed that the two-frequency coupled harmonic currents increase with the increase of control coefficients. The impact of the proportional coefficient is stronger than that of the integral coefficient. When the harmonic frequency is equal to or below 750 Hz, modifying the inner loop control parameters has significant effects on both $\boldsymbol{I}_{\mathrm{anx1}}$ and $\boldsymbol{I}_{\mathrm{anx2}}$.

4) Impacts of Outer Loop Control Parameters: The impacts of outer loop control parameters are shown in Fig. 9. According to Fig. 9, the increase of control coefficients leads to the increase of two-frequency coupled harmonic currents. The proportional coefficient has a stronger impact on harmonic currents than that of the integral coefficient. When the frequency is equal to or below 750 Hz, changing the outer loop control parameters will

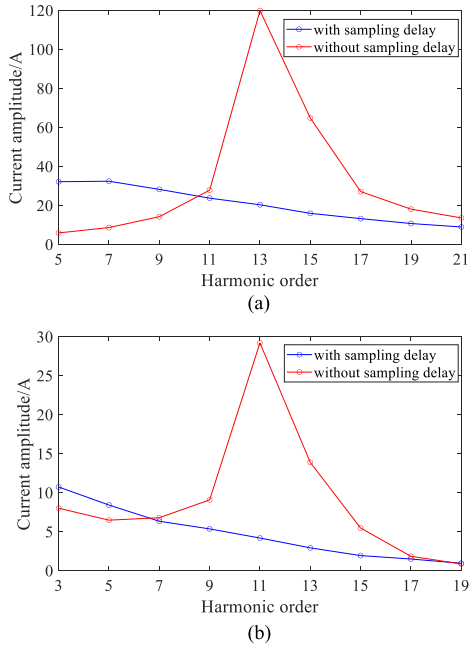

Fig. 7. Impact of sampling delay on the two-frequency currents. (a) I_{anx1}. (b) I_{anx2}.

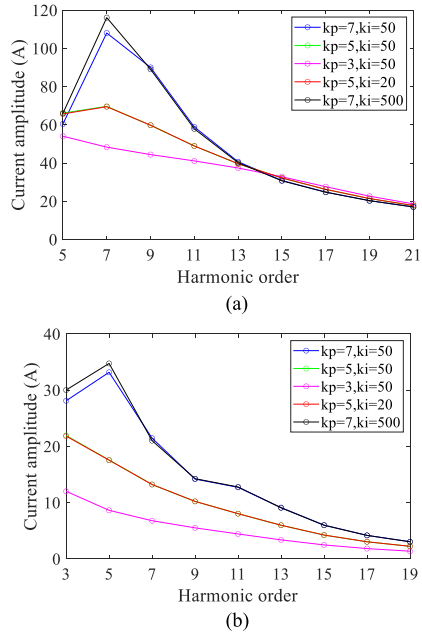

Fig. 8. Impact of inner loop parameters on the two-frequency currents. (a) I_{anx1}. (b) I_{anx2}.

have a relatively noticeable impact on the harmonic currents. In this particular case, when the proportional coefficient exceeds 0.1, the system gradually becomes unstable.

5) Impacts of PLL Parameters: The impacts of PLL parameters are shown in Fig. 10. The impacts of integral coefficient on the two-frequency coupled harmonic currents can be negligible. However, as the proportional coefficient increases, the harmonic currents at both frequencies increase. When the harmonic frequency is equal to or below 550 Hz, altering the

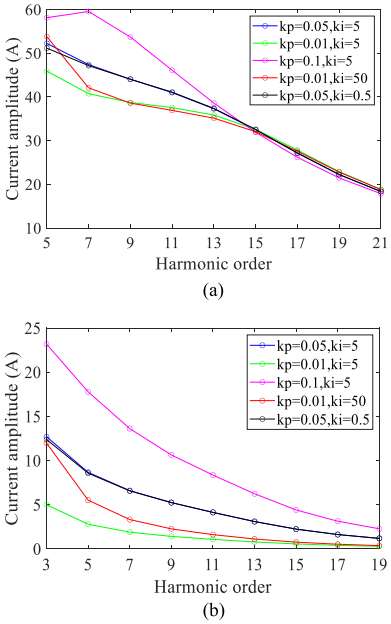

Fig. 9. Impact of out loop parameters on the two-frequency currents. (a) I_{anx1}. (b) I_{anx2}.

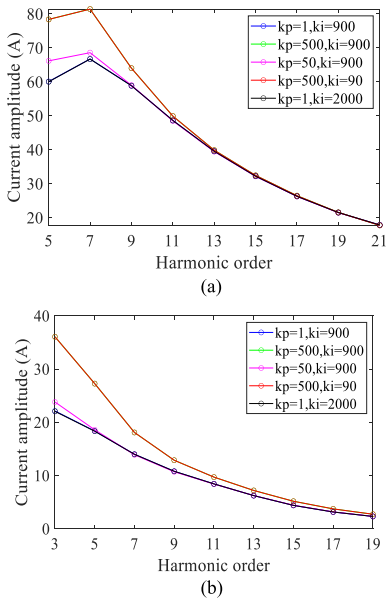

Fig. 10. Impact of PLL parameters on the two-frequency currents. (a) I_{anx1}. (b) I_{anx2}.

proportional coefficient will have relatively pronounced impacts on the two-frequency coupled harmonic currents.

6) Impact of Output Power of GCI: Four values of output active powers are set, respectively, and the impacts of output powers are shown in Fig. 11. The secondary harmonic current I_{anx2} is significantly affected by the output power, increasing as the output power rises. I_{anx1} is less influenced by the output power and primarily affected at frequencies equal to or below 550 Hz.

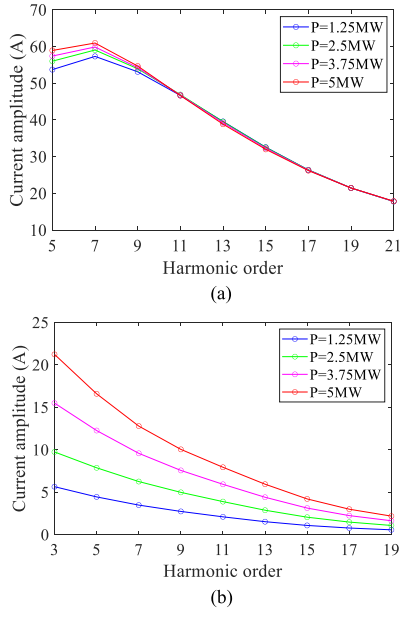

Fig. 11. Impact of output power of GCI on the two-frequency currents. (a) I_{anx1}. (b) I_{anx2}.

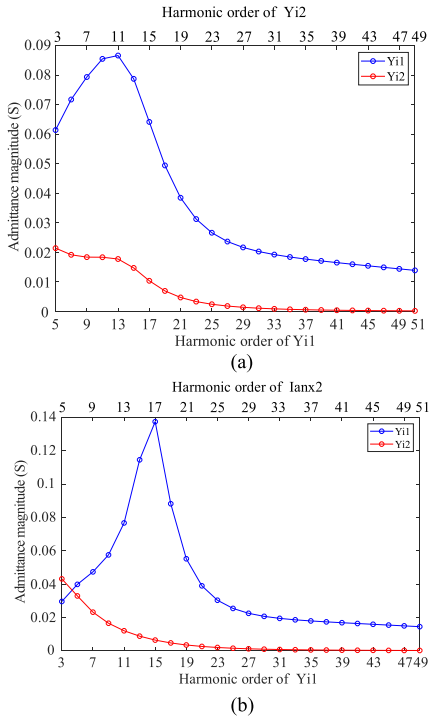

Fig. 12. Two-frequency harmonic admittances of GCI. (a) Positive sequence. (b) Negative sequence.

B. Analysis of the Admittance Characteristics of GCI Under Frequency Coupling Effect

The admittances of GCI, Y_{i1} and Y_{i2} in the models are calculated after applying single odd-order positive and negative-sequence background harmonics, as shown in Fig. 12.

In Fig. 12(a), under positive-sequence background harmonics, Y_{i1} is greater than Y_{i2}. Y_{i1} increases at first then decreases as the harmonic frequency increases and reaches its peak at the 13th

harmonic. Y_{i2} is almost inversely proportional to the harmonic frequency. However, when the harmonic frequency is below 11th, there is not much change in Y_{i2}, which indirectly proves that the frequency coupling effect cannot be ignored when the harmonic frequency is not high.

In Fig. 12(b), under negative-sequence background harmonics, Y_{i1} increases at first then decreases as the harmonic frequency increases and reaches its peak at the 15th harmonic. When the harmonic order is lower than the seventh, Y_{i2} is close to or even higher than Y_{i1}, which further proves the importance of considering the frequency coupling effect in the medium-low frequency range.

VI. Conclusion

This article presents a two-frequency coupled harmonic current source models for GCIs considering the frequency coupling effects caused by *dq*-axis control asymmetry, which accurately calculates the magnitudes and phase angles of harmonic currents grid-connected under background harmonic distortion. The main conclusions are as follows.

1) Considering the interaction of background harmonics and the frequency coupling effect, the harmonic currents of GCIs can be analytically determined. The current source models controlled by the harmonic voltages at PCC are linear under steady-state conditions. Moreover, for the case of multiple background harmonics, the harmonic currents at the same frequency can be vectorially superimposed. Hence, the models presented in this article can be easily integrated into existing harmonic power flow tools.
2) In the bandwidth below 1000 Hz, the frequency coupling effect is more pronounced, and the magnitude of the coupling current cannot be ignored.
3) The parameters of outer loop, inner loop, PLL, and output power of GCI affect the magnitude of the two-frequency coupled harmonic currents. The proportional coefficient of each loop has a stronger impact than that of the integral coefficient.

Appendix A

The Park transformation matrix with disturbance component $\mathbf{P}(\theta_{\mathrm{PLL}})$ is equal to the product of the harmonic component transformation matrix $\mathbf{P_x}(\theta_{\mathbf{x}})$ and the fundamental component transformation matrix $\mathbf{P}(\theta_0)$, as shown in

$$\begin{aligned}\mathbf{P}(\theta_{\mathrm{PLL}}) &= \mathbf{P_x}(\theta_{\mathrm{x}})\cdot\mathbf{P}(\theta_0)\\ &= \begin{bmatrix}\cos(\theta_{\mathrm{x}}) & \sin(\theta_{\mathrm{x}})\\ -\sin(\theta_{\mathrm{x}}) & \cos(\theta_{\mathrm{x}})\end{bmatrix}\\ &\quad\cdot\frac{2}{3}\begin{bmatrix}\cos\theta_0 & \cos(\theta_0-\frac{2\pi}{3}) & \cos(\theta_0+\frac{2\pi}{3})\\ -\sin\theta_0 & -\sin(\theta_0-\frac{2\pi}{3}) & -\sin(\theta_0+\frac{2\pi}{3})\end{bmatrix}.\end{aligned}\tag{A.1}$$

The harmonic component $\theta_{\mathbf{x}}$ caused by grid background disturbance voltage has a relatively small magnitude. It can be mathematically approximated as an infinitesimal transformation on $\mathbf{P_x}(\theta_{\mathbf{x}})$, as shown in

$$\mathbf{P}_{\mathrm{x}}(\theta_{\mathrm{x}}) = \begin{bmatrix}\cos(\theta_{\mathrm{x}}) & \sin(\theta_{\mathrm{x}})\\ -\sin(\theta_{\mathrm{x}}) & \cos(\theta_{\mathrm{x}})\end{bmatrix} \approx \begin{bmatrix}1 & \theta_{\mathrm{x}}\\ -\theta_{\mathrm{x}} & 1\end{bmatrix}.\tag{A.2}$$

$\mathbf{P}^{-1}(\theta_{\mathrm{PLL}})$ can be expressed as the product of the inverse transformation matrix $\mathbf{P}^{-1}(\theta_0)$ for the fundamental frequency and the inverse transformation matrix $\mathbf{P}^{-1}(\theta_{\mathrm{x}})$ for the harmonic components, as shown in

$$\begin{aligned}\mathbf{P}^{-1}(\theta_{PLL}) &= \mathbf{P}^{-1}(\theta_0)\cdot{\mathbf{P}_{\mathrm{x}}}^{-1}(\theta_{\mathrm{x}})\\ &= \begin{bmatrix}\cos\theta_0 & -\sin\theta_0\\ \cos(\theta_0-\frac{2\pi}{3}) & -\sin(\theta_0-\frac{2\pi}{3})\\ \cos(\theta_0+\frac{2\pi}{3}) & -\sin(\theta_0+\frac{2\pi}{3})\end{bmatrix}\\ &\quad\cdot\begin{bmatrix}\cos(\theta_{\mathrm{x}}) & -\sin(\theta_{\mathrm{x}})\\ \sin(\theta_{\mathrm{x}}) & \cos(\theta_{\mathrm{x}})\end{bmatrix}.\end{aligned}\tag{A.3}$$

Appendix B

A. Coefficients of the Model in Sce I

The coefficients $\mathrm{A_{ij}}$ in (17) and $\mathrm{A_i}$ in (23) can be expressed, as shown in (B.1) and (B.2), respectively, as follows:

$$\begin{cases}A_{11} = [-1.5H_{\mathrm{IN}}(\mathrm{j}(\omega_{\mathrm{x1}}-\omega_0))H_{\mathrm{OUT}}(\mathrm{j}(\omega_{\mathrm{x1}}-\omega_0))U_{\mathrm{m0}}\\ \quad -H_{\mathrm{IN}}(\mathrm{j}(\omega_{\mathrm{x1}}-\omega_0))+\mathrm{j}K_{\mathrm{i}}+K_{\mathrm{c}}\omega_{\mathrm{x1}}^2L_2C]\\ \quad K_{\mathrm{PWM}}\mathrm{e}^{-1.5\mathrm{j}T_{\mathrm{s}}\omega_{\mathrm{x1}}}\\ A_{12} = K_{\mathrm{PWM}}(K_{\mathrm{n}}-\mathrm{j}K_{\mathrm{c}}\omega_{\mathrm{x1}}C)\mathrm{e}^{-1.5\mathrm{j}T_{\mathrm{s}}\omega_{\mathrm{x1}}}\\ A_{13} = -1.5K_{\mathrm{PWM}}H_{\mathrm{IN}}(\mathrm{j}(\omega_{\mathrm{x1}}-\omega_0))H_{\mathrm{OUT}}(\mathrm{j}(\omega_{\mathrm{x1}}-\omega_0))\\ \quad *I_{\mathrm{mn0}}\mathrm{e}^{\mathrm{j}\varphi_{\mathrm{in0}}}\mathrm{e}^{-1.5\mathrm{j}T_{\mathrm{s}}\omega_{\mathrm{x}}}\\ A_{14} = 0.5K_{\mathrm{PWM}}\{[K_{\mathrm{i}}+\mathrm{j}H_{\mathrm{IN}}(\mathrm{j}(\omega_{\mathrm{x1}}-\omega_0))]I_{\mathrm{mn0}}\mathrm{e}^{\mathrm{j}\varphi_{\mathrm{in0}}}\\ \quad -\mathrm{j}K_{\mathrm{n}}U_{\mathrm{mn0}}+\mathrm{j}u_{\mathrm{dref0}}-u_{\mathrm{qref0}}\}\\ A_{21} = [-1.5H_{\mathrm{IN}}(\mathrm{j}(\omega_{\mathrm{x1}}-\omega_0))H_{\mathrm{OUT}}(\mathrm{j}(\omega_{\mathrm{x1}}-\omega_0))U_{\mathrm{mn0}}\\ \quad -H_{\mathrm{IN}}(\mathrm{j}(\omega_{\mathrm{x1}}-\omega_0))-\mathrm{j}K_{\mathrm{i}}+K_{\mathrm{c}}\omega_{\mathrm{x1}}^2L_2C]\\ \quad K_{\mathrm{PWM}}\mathrm{e}^{-1.5\mathrm{j}T_{\mathrm{s}}(\omega_{\mathrm{x1}}-2\omega_0)}\\ A_{22} = K_{\mathrm{PWM}}(K_{\mathrm{n}}-\mathrm{j}K_{\mathrm{c}}\omega_{\mathrm{x2}}C)\mathrm{e}^{-1.5\mathrm{j}T_{\mathrm{s}}(\omega_{\mathrm{x1}}-2\omega_0)}\\ A_{23} = -1.5K_{\mathrm{PWM}}H_{\mathrm{IN}}(\mathrm{j}(\omega_{\mathrm{x1}}-\omega_0))H_{\mathrm{OUT}}(\mathrm{j}(\omega_{\mathrm{x1}}-\omega_0))\\ \quad *I_{\mathrm{mn0}}\mathrm{e}^{-\mathrm{j}\varphi_{\mathrm{in0}}}\mathrm{e}^{-1.5\mathrm{j}T_{\mathrm{s}}(\omega_{\mathrm{x1}}-2\omega_0)}\\ A_{24} = 0.5K_{\mathrm{PWM}}\{[K_{\mathrm{i}}-\mathrm{j}H_{\mathrm{IN}}(\mathrm{j}(\omega_{\mathrm{x1}}-\omega_0))]I_{\mathrm{mn0}}\mathrm{e}^{-\mathrm{j}\varphi_{\mathrm{in0}}}\\ \quad +\mathrm{j}K_{\mathrm{n}}U_{\mathrm{mn0}}-\mathrm{j}u_{\mathrm{dref0}}-u_{\mathrm{qref0}}\}\end{cases}\tag{B.1}$$

$$\begin{cases}A_1 = \frac{A_{11}-(R_1+\mathrm{j}\omega_{\mathrm{x1}}L_1+R_2+\mathrm{j}\omega_{\mathrm{x1}}L_2+R_{\mathrm{g}}+\mathrm{j}\omega_{\mathrm{x1}}L_{\mathrm{g}})}{R_{\mathrm{g}}+\mathrm{j}\omega_{\mathrm{x}}L_{\mathrm{g}}}\\ +A_{12}-\frac{(R_1+\mathrm{j}\omega_{\mathrm{x1}}L_1)(R_2+\mathrm{j}\omega_{\mathrm{x1}}L_2+R_{\mathrm{g}}+\mathrm{j}\omega_{\mathrm{x1}}L_{\mathrm{g}})}{(R_c+\frac{1}{\mathrm{j}\omega_{\mathrm{x1}}C})(R_{\mathrm{g}}+\mathrm{j}\omega_{\mathrm{x1}}L_{\mathrm{g}})}\\ \quad -\frac{\mathrm{j}A_{14}H_{\mathrm{PLL}}(\mathrm{j}(\omega_{\mathrm{x1}}-\omega_0))}{\mathrm{j}(\omega_{\mathrm{x1}}-\omega_0)+H_{\mathrm{PLL}}(\mathrm{j}(\omega_{\mathrm{x1}}-\omega_0))U_{\mathrm{mn0}}}\\ A_2 = \frac{R_1+\mathrm{j}\omega_{\mathrm{x1}}L_1+R_2+\mathrm{j}\omega_{\mathrm{x1}}L_2-A_{11}}{R_{\mathrm{g}}+\mathrm{j}\omega_{\mathrm{x}}L_{\mathrm{g}}}\\ \quad +\frac{(R_1+\mathrm{j}\omega_{\mathrm{x1}}L_1)(R_2+\mathrm{j}\omega_{\mathrm{x1}}L_2)}{(R_c+\frac{1}{\mathrm{j}\omega_{\mathrm{x1}}C})(R_{\mathrm{g}}+\mathrm{j}\omega_{\mathrm{x1}}L_{\mathrm{g}})}\\ A_3 = A_{13}+\frac{\mathrm{j}A_{14}H_{\mathrm{PLL}}(\mathrm{j}(\omega_{\mathrm{x1}}-\omega_0))}{\mathrm{j}(\omega_{\mathrm{x1}}-\omega_0)+H_{\mathrm{PLL}}(\mathrm{j}(\omega_{\mathrm{x1}}-\omega_0))U_{\mathrm{mn0}}}\\ A_4 = A_{23}-\frac{\mathrm{j}A_{24}H_{\mathrm{PLL}}(\mathrm{j}(\omega_{\mathrm{x1}}-\omega_0))}{\mathrm{j}(\omega_{\mathrm{x1}}-\omega_0)+H_{\mathrm{PLL}}(\mathrm{j}(\omega_{\mathrm{x1}}-\omega_0))U_{\mathrm{mn0}}}\\ A_5 = \frac{A_{21}-(R_1+\mathrm{j}\omega_{\mathrm{x2}}L_1+R_2+\mathrm{j}\omega_{\mathrm{x2}}L_2+R_{\mathrm{g}}+\mathrm{j}\omega_{\mathrm{x2}}L_{\mathrm{g}})}{R_{\mathrm{g}}+\mathrm{j}\omega_{\mathrm{x2}}L_{\mathrm{g}}}\\ \quad +A_{22}-\frac{(R_1+\mathrm{j}\omega_{\mathrm{x2}}L_1)(R_2+\mathrm{j}\omega_{\mathrm{x2}}L_2+R_{\mathrm{g}}+\mathrm{j}\omega_{\mathrm{x2}}L_{\mathrm{g}})}{(R_c+\frac{1}{\mathrm{j}\omega_{\mathrm{x2}}C})(R_{\mathrm{g}}+\mathrm{j}\omega_{\mathrm{x2}}L_{\mathrm{g}})}\\ \quad +\frac{\mathrm{j}A_{24}H_{\mathrm{PLL}}(\mathrm{j}(\omega_{\mathrm{x1}}-\omega_0))}{\mathrm{j}(\omega_{\mathrm{x1}}-\omega_0)+H_{\mathrm{PLL}}(\mathrm{j}(\omega_{\mathrm{x1}}-\omega_0))U_{\mathrm{mn0}}}.\end{cases}\tag{B.2}$$

B. Coefficients of the Model in Sce II

Equation (B.3) corresponds to the modifications required for the positive-sequence model for frequencies lower than twice the fundamental frequency

$$\begin{cases} A_{11} = [-1.5H_{\mathrm{IN}}(\mathrm{j}(\omega_{\mathrm{x1}}-\omega_0))H_{\mathrm{OUT}}(\mathrm{j}(\omega_{\mathrm{x1}}-\omega_0))U_{\mathrm{m0}} \\ \quad -H_{\mathrm{IN}}(\mathrm{j}(\omega_{\mathrm{x1}}-\omega_0))+\mathrm{j}K_{\mathrm{i}}+K_{\mathrm{c}}\omega_{\mathrm{x1}}^2L_2C] \\ \quad K_{\mathrm{PWM}}\mathrm{e}^{-1.5\mathrm{j}T_{\mathrm{s}}\omega_{\mathrm{x1}}} \\ A_{12} = K_{\mathrm{PWM}}(K_{\mathrm{n}}-\mathrm{j}K_{\mathrm{c}}\omega_{\mathrm{x1}}C)\mathrm{e}^{-1.5\mathrm{j}T_{\mathrm{s}}\omega_{\mathrm{x1}}} \\ A_{13} = -1.5H_{\mathrm{IN}}(\mathrm{j}(\omega_{\mathrm{x1}}-\omega_0))H_{\mathrm{OUT}}(\mathrm{j}(\omega_{\mathrm{x1}}-\omega_0)) \\ \quad * I_{\mathrm{mn0}}\mathrm{e}^{\mathrm{j}\varphi_{\mathrm{in0}}}\mathrm{e}^{-1.5\mathrm{j}T_{\mathrm{s}}\omega_{\mathrm{x1}}} \\ A_{14} = 0.5\{[K_{\mathrm{i}}+\mathrm{j}H_{\mathrm{IN}}(\mathrm{j}(\omega_{\mathrm{x1}}-\omega_0))]I_{\mathrm{mn0}}\mathrm{e}^{\mathrm{j}\varphi_{\mathrm{in0}}} \\ \quad -\mathrm{j}K_{\mathrm{n}}U_{\mathrm{mn0}}+\mathrm{j}u_{\mathrm{dref0}}-u_{\mathrm{qref0}}\} \\ A_{21} = [-1.5H_{\mathrm{IN}}(\mathrm{j}(\omega_{\mathrm{x1}}-\omega_0))H_{\mathrm{OUT}}(\mathrm{j}(\omega_{\mathrm{x1}}-\omega_0))U_{\mathrm{mn0}} \\ \quad -H_{\mathrm{IN}}(\mathrm{j}(\omega_{\mathrm{x1}}-\omega_0))-\mathrm{j}K_{\mathrm{i}}+K_{\mathrm{c}}\omega_{\mathrm{x2}}^2L_2C] \\ \quad \mathrm{e}^{-1.5\mathrm{j}T_{\mathrm{s}}(2\omega_0-\omega_{\mathrm{x1}})} \\ A_{22} = (K_{\mathrm{n}}-\mathrm{j}K_{\mathrm{c}}\omega_{\mathrm{x2}}C)\mathrm{e}^{-1.5\mathrm{j}T_{\mathrm{s}}(2\omega_0-\omega_{\mathrm{x1}})} \\ A_{23} = -1.5H_{\mathrm{IN}}(\mathrm{j}(\omega_{\mathrm{x1}}-\omega_0))H_{\mathrm{OUT}}(\mathrm{j}(\omega_{\mathrm{x1}}-\omega_0)) \\ \quad * I_{\mathrm{mn0}}\mathrm{e}^{-\mathrm{j}\varphi_{\mathrm{in0}}}\mathrm{e}^{-1.5\mathrm{j}T_{\mathrm{s}}(2\omega_0-\omega_{\mathrm{x1}})} \\ A_{24} = 0.5\{[K_{\mathrm{i}}-\mathrm{j}H_{\mathrm{IN}}(\mathrm{j}(\omega_{\mathrm{x1}}-\omega_0))]I_{\mathrm{mn0}}\mathrm{e}^{-\mathrm{j}\varphi_{\mathrm{in0}}} \\ \quad +\mathrm{j}K_{\mathrm{n}}U_{\mathrm{mn0}}-\mathrm{j}u_{\mathrm{dref0}}-u_{\mathrm{qref0}}\}. \end{cases} \tag{B.3}$$

C. Coefficients of the Model in Sce III

The coefficients B_{ij} in (24) and B_i in (26) can be expressed, as shown in (B.4) and (B.5), respectively, as follows:

$$\begin{cases} B_{11} = [-1.5H_{\mathrm{IN}}(\mathrm{j}(\omega_{\mathrm{x1}}+\omega_0))H_{\mathrm{OUT}}(\mathrm{j}(\omega_{\mathrm{x}}+\omega_0))U_{\mathrm{mn0}} \\ \quad -H_{\mathrm{IN}}(\mathrm{j}(\omega_{\mathrm{x}}+\omega_0))-\mathrm{j}K_{\mathrm{i}}+K_{\mathrm{c}}\omega_{\mathrm{x1}}^2L_2C_1] \\ \quad K_{\mathrm{PWM}}\mathrm{e}^{-1.5\mathrm{j}T_{\mathrm{s}}\omega_{\mathrm{x1}}} \\ B_{12} = K_{\mathrm{PWM}}(K_{\mathrm{n}}-\mathrm{j}K_{\mathrm{c}}\omega_{\mathrm{x1}}C_1)\mathrm{e}^{-1.5\mathrm{j}T_{\mathrm{s}}\omega_{\mathrm{x1}}} \\ B_{13} = -1.5K_{\mathrm{PWM}}H_{\mathrm{IN}}(\mathrm{j}(\omega_{\mathrm{x1}}+\omega_0))H_{\mathrm{OUT}}(\mathrm{j}(\omega_{\mathrm{x1}}+\omega_0)) \\ \quad * I_{\mathrm{mn0}}\mathrm{e}^{-\mathrm{j}\varphi_{\mathrm{in0}}}\mathrm{e}^{-1.5\mathrm{j}T_{\mathrm{s}}\omega_{\mathrm{x1}}} \\ B_{14} = 0.5K_{\mathrm{PWM}}\{[-\mathrm{j}H_{\mathrm{IN}}(\mathrm{j}(\omega_{\mathrm{x1}}+\omega_0))+K_{\mathrm{i}}]I_{\mathrm{mn0}}\mathrm{e}^{-\mathrm{j}\varphi_{\mathrm{in0}}} \\ \quad +\mathrm{j}K_{\mathrm{n}}U_{\mathrm{mn0}}-\mathrm{j}u_{\mathrm{dref0}}-u_{\mathrm{qref0}}\} \\ B_{21} = [-1.5H_{\mathrm{IN}}(\mathrm{j}(\omega_{\mathrm{x}}+\omega_0))H_{\mathrm{OUT}}(\mathrm{j}(\omega_{\mathrm{x}}+\omega_0))U_{\mathrm{mn0}} \\ \quad -H_{\mathrm{IN}}(\mathrm{j}(\omega_{\mathrm{x1}}+\omega_0))+\mathrm{j}K_{\mathrm{i}}+K_{\mathrm{c}}\omega_{\mathrm{x1}}^2L_2C_1] \\ \quad K_{\mathrm{PWM}}\mathrm{e}^{-1.5\mathrm{j}T_{\mathrm{s}}(\omega_{\mathrm{x1}}+2\omega_0)} \\ B_{22} = K_{\mathrm{PWM}}(K_{\mathrm{n}}-\mathrm{j}K_{\mathrm{c}}\omega_{\mathrm{x2}}C_1)\mathrm{e}^{-1.5\mathrm{j}T_{\mathrm{s}}(\omega_{\mathrm{x1}}+2\omega_0)} \\ B_{23} = -1.5K_{\mathrm{PWM}}H_{\mathrm{IN}}(\mathrm{j}(\omega_{\mathrm{x1}}+\omega_0))H_{\mathrm{OUT}}(\mathrm{j}(\omega_{\mathrm{x1}}+\omega_0)) \\ \quad * I_{\mathrm{mn0}}\mathrm{e}^{\mathrm{j}\varphi_{\mathrm{in0}}}\mathrm{e}^{-1.5\mathrm{j}T_{\mathrm{s}}(\omega_{\mathrm{x1}}+2\omega_0)} \\ B_{24} = 0.5K_{\mathrm{PWM}}\{[\mathrm{j}H_{\mathrm{IN}}(\mathrm{j}(\omega_{\mathrm{x1}}+\omega_0))+K_{\mathrm{i}}]I_{\mathrm{mn0}}\mathrm{e}^{\mathrm{j}\varphi_{\mathrm{in0}}} \\ \quad -\mathrm{j}K_{\mathrm{n}}U_{\mathrm{mn0}}+\mathrm{j}u_{\mathrm{dref0}}-u_{\mathrm{qref0}}\} \end{cases} \tag{B.4}$$

$$\begin{cases} B_1 = \frac{B_{11}-(R_1+\mathrm{j}\omega_{\mathrm{x1}}L_1+R_2+\mathrm{j}\omega_{\mathrm{x1}}L_2+R_{\mathrm{g}}+\mathrm{j}\omega_{\mathrm{x1}}L_{\mathrm{g}})}{R_{\mathrm{g}}+\mathrm{j}\omega_{\mathrm{x1}}L_{\mathrm{g}}} \\ \quad +B_{12}-\frac{(R_1+\mathrm{j}\omega_{\mathrm{x1}}L_1)(R_2+\mathrm{j}\omega_{\mathrm{x1}}L_2+R_{\mathrm{g}}+\mathrm{j}\omega_{\mathrm{x1}}L_{\mathrm{g}})}{(R_c+B_1)(R_{\mathrm{g}}+\mathrm{j}\omega_{\mathrm{x1}}L_{\mathrm{g}})} \\ \quad +\frac{\mathrm{j}B_{14}H_{\mathrm{PLL}}(\mathrm{j}(\omega_{\mathrm{x1}}+\omega_0))}{\mathrm{j}(\omega_{\mathrm{x1}}+\omega_0)+H_{\mathrm{PLL}}(\mathrm{j}(\omega_{\mathrm{x1}}+\omega_0))U_{\mathrm{mn0}}} \\ B_2 = \frac{R_1+\mathrm{j}\omega_{\mathrm{x1}}L_1+R_2+\mathrm{j}\omega_{\mathrm{x1}}L_2-B_{11}}{R_{\mathrm{g}}+\mathrm{j}\omega_{\mathrm{x}}L_{\mathrm{g}}} \\ \quad +\frac{(R_1+\mathrm{j}\omega_{\mathrm{x1}}L_1)(R_2+\mathrm{j}\omega_{\mathrm{x1}}L_2)}{(R_c+B_1)(R_{\mathrm{g}}+\mathrm{j}\omega_{\mathrm{x1}}L_{\mathrm{g}})} \\ B_3 = B_{13}-\frac{\mathrm{j}B_{14}H_{\mathrm{PLL}}(\mathrm{j}(\omega_{\mathrm{x1}}+\omega_0))}{\mathrm{j}(\omega_{\mathrm{x1}}+\omega_0)+H_{\mathrm{PLL}}(\mathrm{j}(\omega_{\mathrm{x1}}+\omega_0))U_{\mathrm{mn0}}} \\ B_4 = B_{23}+\frac{\mathrm{j}B_{24}H_{\mathrm{PLL}}(\mathrm{j}(\omega_{\mathrm{x1}}+\omega_0))}{\mathrm{j}(\omega_{\mathrm{x1}}+\omega_0)+H_{\mathrm{PLL}}(\mathrm{j}(\omega_{\mathrm{x1}}+\omega_0))U_{\mathrm{mn0}}} \\ B_5 = \frac{B_{21}-(R_1+\mathrm{j}\omega_{\mathrm{x2}}L_1+R_2+\mathrm{j}\omega_{\mathrm{x2}}L_2+R_{\mathrm{g}}+\mathrm{j}\omega_{\mathrm{x2}}L_{\mathrm{g}})}{R_{\mathrm{g}}+\mathrm{j}\omega_{\mathrm{x2}}L_{\mathrm{g}}} \\ \quad +B_{22}-\frac{(R_1+\mathrm{j}\omega_{\mathrm{x2}}L_1)(R_2+\mathrm{j}\omega_{\mathrm{x2}}L_2+R_{\mathrm{g}}+\mathrm{j}\omega_{\mathrm{x2}}L_{\mathrm{g}})}{(R_c+B_2)(R_{\mathrm{g}}+\mathrm{j}\omega_{\mathrm{x2}}L_{\mathrm{g}})} \\ \quad +\frac{\mathrm{j}B_{24}H_{\mathrm{PLL}}(\mathrm{j}(\omega_{\mathrm{x1}}+\omega_0))}{\mathrm{j}(\omega_{\mathrm{x1}}+\omega_0)+H_{\mathrm{PLL}}(\mathrm{j}(\omega_{\mathrm{x1}}+\omega_0))U_{\mathrm{mn0}}}. \end{cases} \tag{B.5}$$

REFERENCES

[1] Z. Tang, Y. Yang, and F. Blaabjerg, "Power electronics: The enabling technology for renewable energy integration," *CSEE J. Power Energy Syst.*, vol. 8, no. 1, pp. 39–52, Jan. 2022.

[2] T. Muhammad et al., "An adaptive hybrid control of reduced switch multilevel grid connected inverter for weak grid applications," *IEEE Access*, vol. 11, pp. 28103–28118, 2023.

[3] H. Hu, Y. Zhou, X. Li, and K. Lei, "Low-frequency oscillation in Electric Railway Depot: A comprehensive review," *IEEE Trans. Power Electron.*, vol. 36, no. 1, pp. 295–314, Jan. 2021..

[4] X. Wang, M. G. Taul, H. Wu, F. Blaabjerg, and L. Harnefors, "Grid-synchronization stability of converter-based resources—An overview," *IEEE Open J. Ind. Appl.*, vol. 1, pp. 115–134, Aug. 31, 2020.

[5] Y. Song and F. Blaabjerg, "Overview of DFIG-based wind power system resonances under weak networks," *IEEE Trans. Power Electron.*, vol. 32, no. 6, pp. 4370–4394, Jun. 2017.

[6] Q. Liu, F. Liu, R. Zou, and Y. Li, "Harmonic resonance characteristic of large-scale PV plant: Modelling, analysis, and engineering case," *IEEE Trans. Power Del.*, vol. 37, no. 3, pp. 2359–2368, Jun. 2022.

[7] N. Jiao, S. Wang, T. Liu, Y. Wang, and Z. Chen, "Harmonic quantitative analysis for dead-time effects in SPWM inverters," *IEEE Access*, vol. 7, pp. 43143–43152, 2019.

[8] E. Guest, K. H. Jensen, and T. W. Rasmussen, "Sequence domain harmonic modeling of type-IV wind turbines," *IEEE Trans. Power Electron.*, vol. 33, no. 6, pp. 4934–4943, Jun. 2018.

[9] N. Xie et al., "Dynamic modeling and characteristic analysis on harmonics of photovoltaic power stations," *Proc. Chin. Soc. Elect. Eng.*, vol. 33, no. 36, pp. 10–17, 2013.

[10] Y. Xu, H. Nian, T. Wang, L. Chen, and T. Zheng, "Frequency coupling characteristic modeling and stability analysis of doubly fed induction generator," *IEEE Trans. Energy Convers.*, vol. 33, no. 3, pp. 1475–1486, Sep. 2018.

[11] X. Zhang, S. Fu, W. Chen, N. Zhao, G. Wang, and D. Xu, "A symmetrical control method for grid-connected converters to suppress the frequency coupling under weak grid conditions," *IEEE Trans. Power Electron.*, vol. 35, no. 12, pp. 13488–13499, Dec. 2020.

[12] S. Song, Z. Wei, Y. Lin, B. Liu, and H. Liu, "Impedance modeling and stability analysis of PV grid-connected inverter systems considering frequency coupling," *CSEE J. Power Energy Syst.*, vol. 6, no. 2, pp. 279–290, Jun. 2020.

[13] S. Xu, Y. Xu, S. Tao, S. Zhou, and W. Zhou, "Research on sampling and PWM sideband secondary harmonic characteristics of grid connected converter," *Proc. Chin. Soc. Elect. Eng.*, vol. 43, no. 11, pp. 4340–4354, 2023.

[14] B. Gao, Y. Wang, and W. Xu, "Modeling voltage source converters for harmonic power flow studies," *IEEE Trans. Power Del.*, vol. 36, no. 6, pp. 3426–3437, Dec. 2021.

[15] Z Ye et al., "Admittance modeling and stability enhancement of grid-connected inverter considering frequency coupling in weak grids," *Electric Power Syst. Res.*, vol. 209, 2022, doi: 10.1016/j.epsr.2022.108034.

[16] W. Liu, Z. Lu, X. Wang, and X. Xie, "Frequency-coupled admittance modelling of grid-connected voltage source converters for the stability evaluation of subsynchronous interaction," *IET Renewable Power Gener.*, vol. 13, pp. 285–295, 2019.

[17] H. Nian, Y. Xu, L. Chen, and G. Li, "Frequency coupling characteristic modeling of grid-connected inverter and system stability analysis," *Proc. Chin. Soc. Elect. Eng.*, vol. 39, no. 5, pp. 1421–1431, 2019.
[18] X. Wang, A. Yang, Y. Liu, and X. Zhao, "Stability control study of grid-connected inverters considering frequency coupling effect," *Power Syst. Technol.*, vol. 47, no. 8, pp. 3280–3288, 2023.
[19] J. Sun, "Two-port characterization and transfer immittances of AC-DC converters—Part I: Modeling," *IEEE Open J. Power Electron.*, vol. 2, pp. 440–462, Aug. 12, 2021.
[20] Y. Cai, Y. He, H. Zhang, H. Zhou, and J. Liu, "Research on harmonic State-space modeling and calculation analysis of low-switching-frequency grid-connected inverter considering the impact of digitization," *IEEE Trans. Power Electron.*, vol. 38, no. 1, pp. 1003–1021, Jan. 2023.
[21] P. Rodriguez, J. Pou, J. Bergas, J. I. Candela, R. P. Burgos, and D. Boroyevich, "Decoupled double synchronous reference frame PLL for power converters control," *IEEE Trans. Power Electron.*, vol. 22, no. 2, pp. 584–592, Mar. 2007.
[22] S. Golestan, J. M. Guerrero, and J. C. Vasquez, "Three-phase PLLs: A review of recent advances," *IEEE Trans. Power Electron.*, vol. 32, no. 3, pp. 1894–1907, Mar. 2017.
[23] A. Rygg, M. Molinas, C. Zhang, and X. Cai, "A modified sequence-domain impedance definition and its equivalence to the dq-domain impedance definition for the stability analysis of AC Power Electronic Systems," *IEEE J. Emerg. Sel. Topics Power Electron.*, vol. 4, no. 4, pp. 1383–1396, Dec. 2016.
[24] F. Xing, Z. Xu, H. Xiao, and Z. Zhang, "Analysis on response characteristics of two-level VSC to disturbances and its oscillation suppression strategy," *J. Elect. Eng. Technol.*, vol. 16, no. 3, pp. 1389–1401, 2021.
[25] J. Sun, "Two-port characterization and transfer immittances of AC-DC converters–Part II: Applications," *IEEE Open J. Power Electron.*, vol. 2, pp. 483–510, Aug. 12, 2021.
[26] S. Haykin, *Communication Systems,* 5th ed. Hoboken, NJ, USA: Wiley, 2007.
[27] W. Liu, Z. Lu, X. Wang, and X. Xie, "Frequency-coupled admittance modelling of grid-connected voltage source converters for the stability evaluation of sub-synchronous interaction," *IET Renewable Power Gener.*, vol. 13, pp. 285–295, 2019.
[28] Y. Liao, Z. Liu, H. Zhang, and B. Wen, "Low-frequency stability analysis of single-phase system with dq-frame impedance approach—Part I: Impedance modeling and verification," *IEEE Trans. Ind. Appl.*, vol. 54, no. 5, pp. 4999–5011, Sep./Oct. 2018.
[29] J. Sun, "Frequency-domain stability criteria for converter-based power systems," *IEEE Open J. Power Electron.*, vol. 3, pp. 222–254, Mar. 1, 2022.

Shun Tao (Member, IEEE) was born in China, in 1972. She received the M.S. and Ph.D. degrees in electrical engineering from North China Electric Power University (NCEPU), Beijing, China, in 2005 and 2008, respectively.

She had a Postdoc procedure with the Electrical Engineering Laboratory de Grenoble, Institute National Polytechnique de Grenoble, Grenoble, France, in 2010. She has been with the NCEPU since 2008. Her research interests include active distribution network and its power-quality.

Xinyi Zhu was born in Quzhou, China, in 2000. He received the B.S. degree in electric power system and automation from Yanshan University, Qinhuangdao, China, in 2022. He is currently working toward the M.S. degree in electrical engineering with North China Electric Power University, Beijing, China.

His research interests include analysis and control of new energy power quality.

Shaobo Xu was born in China in 1994. He received the bachelor's degree in electrical engineering in 2017 from North China Electric Power University, Beijing, China, where he is currently working toward the Doctoral degree in electrical engineering.

His research interests include active distribution network and its power-quality.

Yonghai Xu (Member, IEEE) was born in Xinye, China, in 1966. He received the B.S. degree in electrical engineering from Tsinghua University, Beijing, China, in 1989, the M.S. degree in electrical engineering from North China Electric Power University, Beijing, in 1992 and the Ph.D. degree in electrical engineering from the Harbin Institute of Technology, Harbin, China, in 2002.

He is currently a Professor with the School of Electrical and Electronic Engineering, North China Electric Power University. His research interests include power quality analysis and control, and new energy power system.